



# Experimental measurements and numerical simulations to evaluate the electrode kinetics for 316 stainless steel under PWR-relevant conditions

Marc Vankeerberghen\*, Serguei Gavrilov

SCK · CEN, Nuclear Materials Science Institute, Boeretang 200, 2400 Mol, Belgium

## ARTICLE INFO

### Article history:

Received 21 December 2007

Accepted 10 March 2008

### PACS:

82.45

## ABSTRACT

The local environment in an occluded region of a pressurized water reactor (PWR) depends on its geometry, its access to the bulk and the nature of the electrode kinetics at the metal surfaces. In PWR-relevant, oxygen-free, boric acid–lithium hydroxide solutions the dominant anodic and cathodic electrode reactions are found to be hydrogen oxidation and water reduction, respectively. The hydrogen oxidation reaction kinetics have been quantified using potentiostatic measurements – at 300 °C, under various dissolved hydrogen concentrations, for 1000 ppmB and 2 ppmLi. The reaction kinetics have been verified by modelling of a crevice experiment performed in an autoclave at 300 °C for 1000 ppmB, 2 ppmLi and 25 STP ccH<sub>2</sub>/kg.

© 2008 Elsevier B.V. All rights reserved.

## 1. Introduction

One form of environmental degradation of in-core components in light water nuclear reactors is irradiation-assisted stress corrosion cracking (IASCC). IASCC is a complex interaction between a stressed material and its environment under the influence of radiation [1,2]. In principle, it is a mechanico-electrochemical process since both IASCC initiation and propagation depend on the stresses and the local environment to which the components are exposed. For boiling water reactors (BWR) it has been reported extensively [3–5] that in cracks and crevices the local environment can deviate significantly from the bulk environment. This deviation is brought about by the occluded region's geometry and the nature of the electrode kinetics. In pressurized water reactors (PWR) boric acid and lithium hydroxide are added to the primary coolant. The former is added for reactivity control whilst the latter is added for pH control, resulting in a substantial buffering of the solution. In order to evaluate the buffering effect in occluded regions [2] the electrode kinetics for 316 stainless steel under PWR-relevant conditions have been studied and then applied to an autoclave crevice. In a first instance potentiostatic electrochemical measurement have been performed to identify and quantify the dominant electrode reactions on 316 stainless steel in PWR-relevant, oxygen-free, boric acid–lithium hydroxide solutions. Then the quantified electrode kinetics have been used to compute the electrochemical conditions inside an autoclave crevice. Last the calculated results have been compared to experimental measurements inside an autoclave crevice.

## 2. Polarisation curve measurements

The electrodes used for potentiostatic and potentiodynamic electrokinetic measurements were in the form of cylinders of 5 mm diameter and 15 mm height and were made of 316 stainless steel. These working electrodes were suspended in an autoclave connected to a circulation loop and their potential was measured against an internal reference electrode (IRE). The IRE is an yttrium stabilised zirconium (YSZ) electrode [7]. Experimental potential versus current density data for the 316 stainless steel in a nominal boric acid–lithium hydroxide solution of 1000 ppmB and 2 ppmLi at 300 °C corresponding to a  $\text{pH}_T = 6.95$ , are given in Figs. 1–5<sup>1</sup> for various dissolved hydrogen concentration. Each of the figures contains various curves. The small dots represent a potentiodynamic scan from the cathodic to the anodic part at a scan rate of 10 mV/min (0.1667 V/s). The large dots represent potentiostatic data points at various applied potentials in the anodic region. The other curves in the graphs will be labelled later, as they are the result of calculations detailed further on. The electrochemical measurements have been performed using a Gamry potentiostat system.

## 3. Autoclave crevice set-up

The autoclave crevice device (Fig. 6) is developed from the Schneider et al. device [6]. The crevice is formed by two parallel, circular surfaces of about 50 mm diameter. The top wall of the crevice is formed by a 316 stainless steel disc which is inserted into a Teflon, insulating holder. The disc is electrically connected to the

\* Corresponding author.

E-mail address: [mvankeer@sckcen.be](mailto:mvankeer@sckcen.be) (M. Vankeerberghen).

<sup>1</sup> For interpretation of colour in Figs. 1–5 and 13 the reader is referred to the web version of this article.

### Nomenclature

$F$	Faradays' constant (C/mol)	$c$	cathodic (with $i$ )
$R$	universal gas constant (J/mol/K)	pas	passive (with $i$ )
$T$	temperature (K)	act	active (with $i$ )
$[H_2]$	hydrogen concentration (mol/m <sup>3</sup> )	$f$	forward (with $k$ )
$E$	electrode potential (V)	$b$	backward (with $k$ )
$i$	current density (A/m <sup>2</sup> )	Pt	platinum sensor (with $E$ )
$\varepsilon$	field strength in oxide (V/m)	WE	work electrode, disc-like specimen (with $E$ )
$\alpha$	charge transfer coefficient (-)	ire	internal reference electrode (with $E$ )
$k$	reaction rate constant	she	standard hydrogen electrode (with $E$ )
$D$	diffusion coefficient (m <sup>2</sup> /s)	HR	hydrogen reaction
$z$	charge number (-)	WR	water reaction
$U$	solution potential (V)	$j$	species number (Nernst-Planck equation)
$C$	concentration (mol/m <sup>3</sup> )		

### Sub- and superscripts

a anodic (with  $i$ )

working electrode input of the electrochemical measurement equipment and electrically insulated from the autoclave body and equipment. The bottom wall of the crevice is formed by a Teflon, insulating holder. The relative distance between the top and bottom walls of the crevice can be altered by the pull rod of the autoclave's slow strain rate device. The bottom holder contains penetrations for various sensors and a central flow channel. Five radially spaced platinum electrodes are installed flush with the

bottom, insulated crevice wall (Fig. 6(b)). They serve to measure the radial potential distribution in the crevice. Below they are referred to as Pt1 to Pt5 where Pt1 is the innermost platinum sensor and Pt5 is the outermost platinum sensor. They are spirally located at radii of 7, 11, 15, 19 and 23 mm from the centre, respectively. All platinum sensor potentials are measured against the internal reference electrode (IRE). The IRE is an yttrium stabilised zirconium (YSZ) electrode [7]. The open circuit potential (OCP) of the

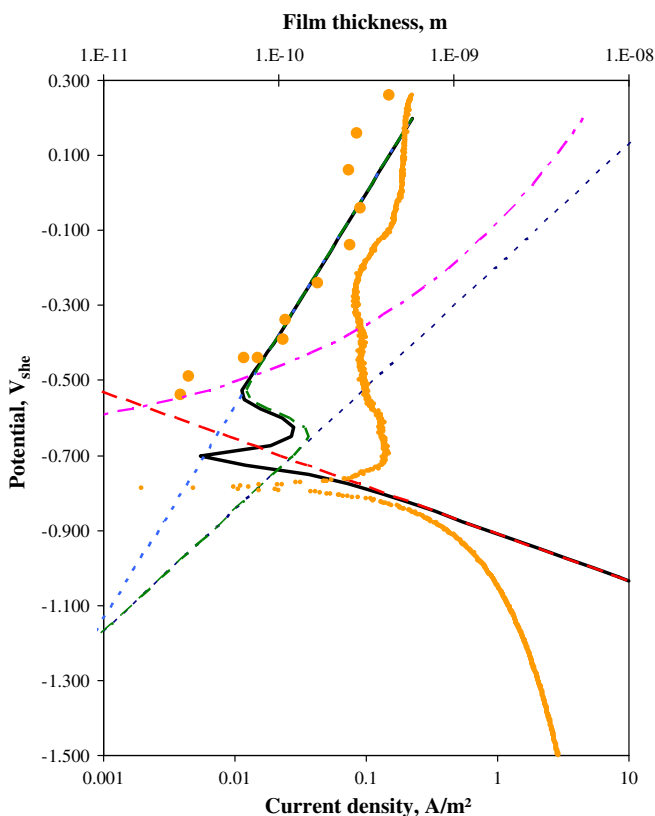


**Fig. 1.** Potential-current density relation for SS316 in an aqueous boron/lithium solution (1000 ppmB, 2 ppmLi) at 300 °C with no hydrogen. The large dots represent potentiostatic measurements. The small dots represent a potentiodynamic scan at 0.1667 mV/s from cathodic to anodic. The long-dashed and solid lines respectively represent the calculated cathodic/anodic and total current density. The dash-dotted curve represents the calculated film thickness. The short-dashed lines represent the anodic hydrogen current on bare metal and on the film.

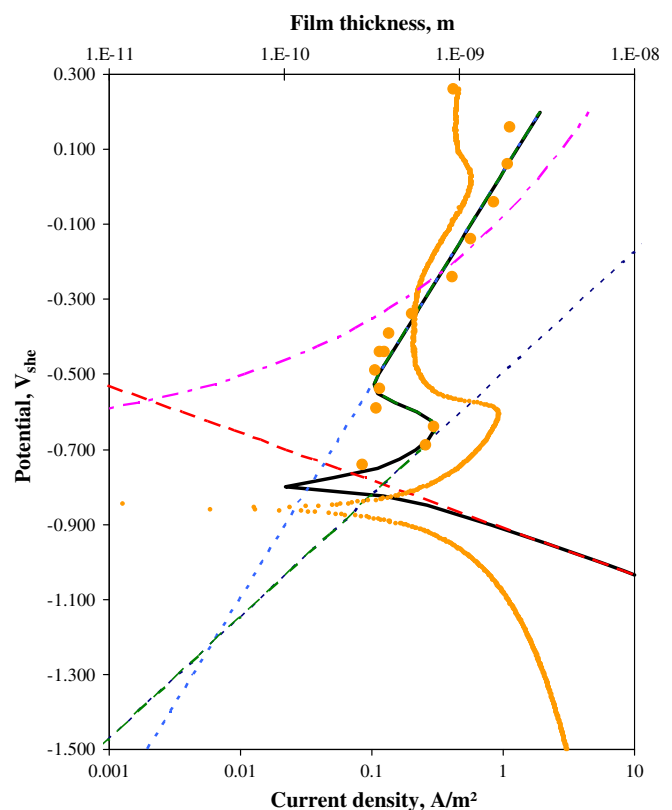


**Fig. 2.** Potential-current density relation for SS316 in an aqueous boron/lithium solution (1000 ppmB, 2 ppmLi) at 300 °C with 17 cc/kg hydrogen. The large dots represent potentiostatic measurements. The small dots represent a potentiodynamic scan at 0.1667 mV/s from cathodic to anodic. The long-dashed and solid lines respectively represent the calculated cathodic/anodic and total current density. The dash-dotted curve represents the calculated film thickness. The short-dashed lines represent the anodic hydrogen current on bare metal and on the film.

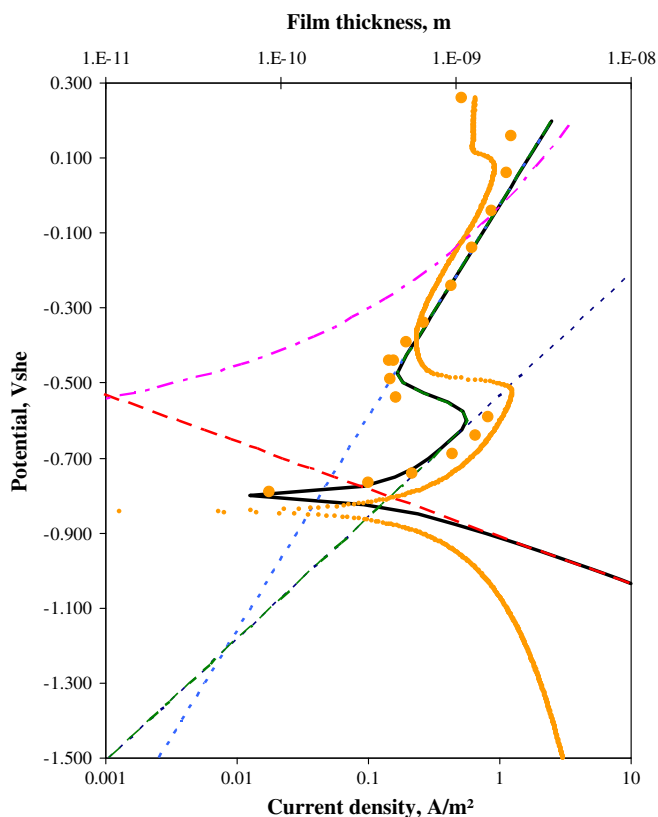


**Fig. 3.** Potential-current density relation for SS316 in an aqueous boron/lithium solution (1000 ppmB, 2 ppmLi) at 300 °C with 22 cc/kg hydrogen. The large dots represent potentiostatic measurements. The small dots represent a potentiodynamic scan at 0.1667 mV/s from cathodic to anodic. The longly-dashed and solid lines respectively represent the calculated cathodic/anodic and total current density. The dash-dotted curve represents the calculated film thickness. The shortly-dashed lines represent the anodic hydrogen current on bare metal and on the film.

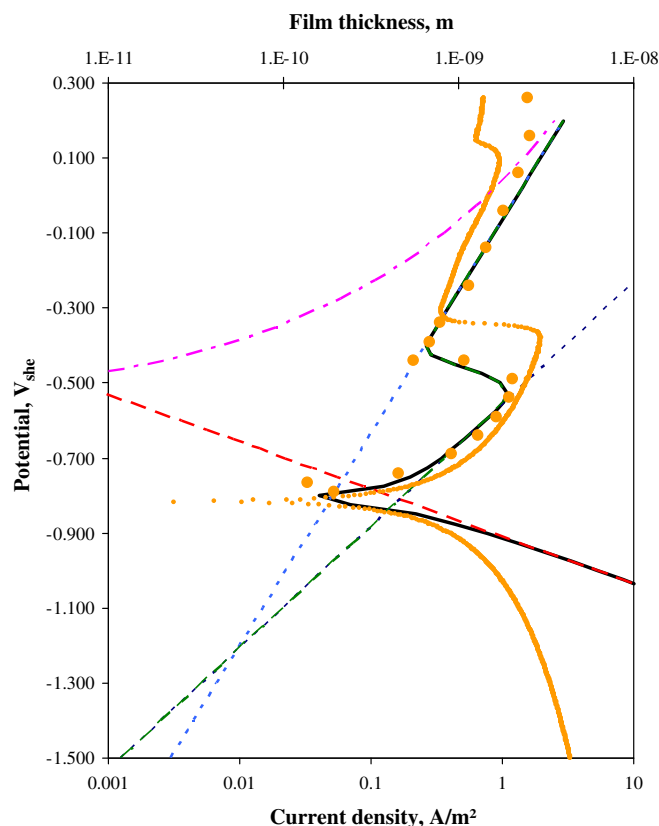


**Fig. 4.** Potential-current density relation for SS316 in an aqueous boron/lithium solution (1000 ppmB, 2 ppmLi) at 300 °C with 26 cc/kg hydrogen. The large dots represent potentiostatic measurements. The small dots represent a potentiodynamic scan at 0.1667 mV/s from cathodic to anodic. The longly-dashed and solid lines respectively represent the calculated cathodic/anodic and total current density. The dash-dotted curve represents the calculated film thickness. The shortly-dashed lines represent the anodic hydrogen current on bare metal and on the film.

specimen making up the top wall of the crevice is measured against the IRE and potentials applied to the specimen are with respect to the IRE. The electrochemical measurements are performed using an HP 34970A Data Acquisition/Switch Unit. The data are read by Agilent Benchlink Data Logger Version 1.4 from where they are exported to a tab-delimited text file which can be read by MS-Excel. Potentials are applied using a Wenking TG 97 Potentiostat/Galvanostat. The crevice height is calibrated at temperature by moving the top and bottom part of the crevice towards each other using the autoclave's pull rod and zeroing the crevice height when the load cell's measured force starts to increase upon contact.

#### 4. Quantification of the reaction kinetics

The model to describe the electrode kinetics on 316 stainless steel in a nominal boric acid–lithium hydroxide solution of 1000 ppmB and 2 ppmLi at 300 °C is based on the mixed potential model [8] and electron conductance through the oxide as per the mixed conduction model [9] and the tunnelling of electrons [10]. The model is described in 'Appendix A'. Another model, associating the current density peak to anodic current density changes, has been discarded. The peak in current density is too large when compared to a visual inspection of the surface after exposure. Indeed, there are no traces of the corrosion products that would normally be associated with such large anodic current densities. Furthermore the peak current density increases with the dissolved hydrogen concentration. Hence, it is believed that the peak in the current density is related to changes in the electron transport through the film, of electrons associated with the hydrogen redox reaction.

The model has been fitted to the potentiostatic data points, the orange dots, in Figs. 1–5. The red, green and black lines in these figures, respectively, represent the calculated cathodic (5), anodic (6) and total current density (3) as a function of the potential. The purple curve represents the calculated film thickness based on tunnelling (14). The dashed blue lines represent the anodic hydrogen current on the bare metal (11) and on the film (12) – the line with the lowest current density being associated with the film.

In essence, the presented model, fitted to the potentiostatic data, yields that the dominant anodic reaction is the hydrogen reaction. Most of the current density is carried by this reaction and the current density carried by anodic dissolution of the material is negligible.

It turns out that film growth is important, but not because of the contribution of the film growth processes to the current. For the latter the ionic current associated with the film growth processes is too small relative to the electronic current. However, film growth is important for its capacity to let through electronic current and to switch from electron transport by tunnelling to electron transport through mixed conduction. This switching is needed to explain the current density peak in the *potential versus current density* data in the anodic region.

#### 5. Modelling of the electrochemistry in the autoclave crevice

Six homogeneous reactions are associated with the aqueous boric acid–lithium hydroxide solution. The reactions and their rate constants are given in the section 'chemical reactions' of Table 3.

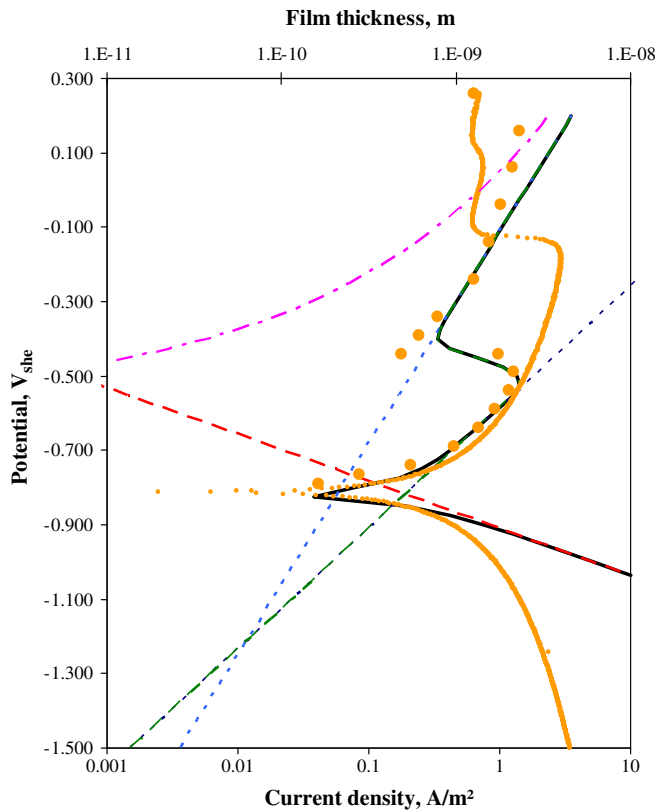


**Fig. 5.** Potential-current density relation for SS316 in an aqueous boron/lithium solution (1000 ppmB, 2 ppmLi) at 300 °C with 31.5 cc/kg hydrogen. The large dots represent potentiostatic measurements. The small dots represent a potentiodynamic scan at 0.1667 mV/s from cathodic to anodic. The longly-dashed and solid lines respectively represent the calculated cathodic/anodic and total current density. The dash-dotted curve represents the calculated film thickness. The shortly-dashed lines represent the anodic hydrogen current on bare metal and on the film.

The species involved in these reactions are listed in the section ‘ion system’ of Table 3. Dilute solution theory [13] is used to model the electrochemistry inside the crevice. This theory describes the transport of ionic species due to diffusion, migration and convection in a dilute aqueous solution. The equations that mathematically describe this transport are called Nernst–Planck equations. There is one Nernst–Planck equation for each species  $j$  in the system

$$\frac{\partial C_j}{\partial t} = D_j \nabla^2 C_j + \frac{F}{RT} z_j D_j \nabla(C_j \nabla U) + R_j, \quad \forall \text{ species } j, \quad (1)$$

where the subscript  $j$  refers to the species’ number,  $C_j$  is the concentration,  $D_j$  the diffusion coefficient,  $z_j$  the charge and  $R_j$  the production rate for species  $j$ ,  $U$  the solution potential and  $R$ ,  $F$  and  $T$  have their usual meaning. The  $D_j$ ,  $z_j$  and  $R_j$  values are listed in the sections ‘ion system’ and ‘production rate’ of Table 3, respectively.

The solution potential used in the Nernst–Planck equations is a field variable too and, hence, an extra equation – the electroneutrality condition – is used to solve for it.

$$\sum_{\text{species}} z_j C_j = 0. \quad (2)$$

Boundary conditions include symmetry at the centre of the axisymmetric crevice and Dirichlet boundary conditions (fixed values) at the mouth of the crevice (Fig. 8) for the concentrations (listed as bulk concentrations in the section ‘ion system’ of Table 3) and potential (zero). At the surface of the stainless steel specimen a Neumann boundary condition (Butler–Volmer equation) is used. The electrode reactions and their associated current densities are given in the section ‘electrochemical reactions’ of Table 3.

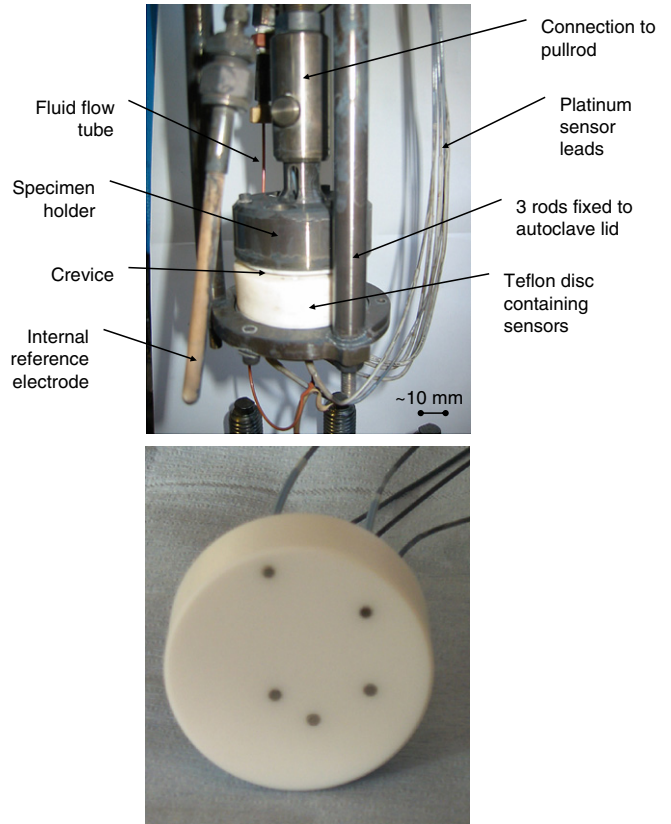


**Fig. 6.** Picture of the autoclave crevice device after the first testing campaign (above) and location of the platinum sensors in the Teflon disc (below).

The system of simultaneous partial differential equations is solved using Comsol Multiphysics. The specification of the system that is modelled is given in Table 3. The environmental conditions specified in the modelling correspond to those of the experiment described above, i.e. 300 °C, 1000 ppmB, 2 ppmLi and 25 cc/kg (STP) dissolved hydrogen.

The results of the calculations are pictured in Figs. 9–12. The lines in Fig. 9 show calculated polarization curves for crevice heights of 250 μm, 500 μm, 1000 μm and 2000 μm. Fig. 10 shows the calculated radial pH profile along the active and non-active parts of the crevice wall for a crevice height of 500 μm. Four curves are shown, corresponding to the experimental conditions of OCP, OCP + 100 mV, OCP + 200 mV and OCP + 300 mV. The distance on the abscissa is measured from the centre of the crevice outwards, 0.025 corresponds to the radius of the disc-like specimen and 0.0275 is the radius of the crevice. Between 0.025 and 0.0275 the wall of the crevice consists of an insulator. Fig. 11 shows the calculated radial electrode potential profile along the active part of the crevice wall for a crevice height of 500 μm. Four curves are shown, corresponding to the experimental conditions of OCP, OCP + 100 mV, OCP + 200 mV and OCP + 300 mV. Fig. 12 shows the calculated radial hydrogen concentration profile along the crevice wall for a crevice height of 500 μm. Four curves are shown, corresponding to the experimental conditions of OCP, OCP + 100 mV, OCP + 200 mV and OCP + 300 mV.

The following conclusions can be made based on the calculated results presented in Figs. 9–12:

- The calculated OCP is about  $-760 \text{ mV}_{\text{she}}$  for all crevice heights.
- The calculated crevice current decreases with the crevice height at all applied potentials. This corresponds to the increased internal resistance of the crevice to current transport.

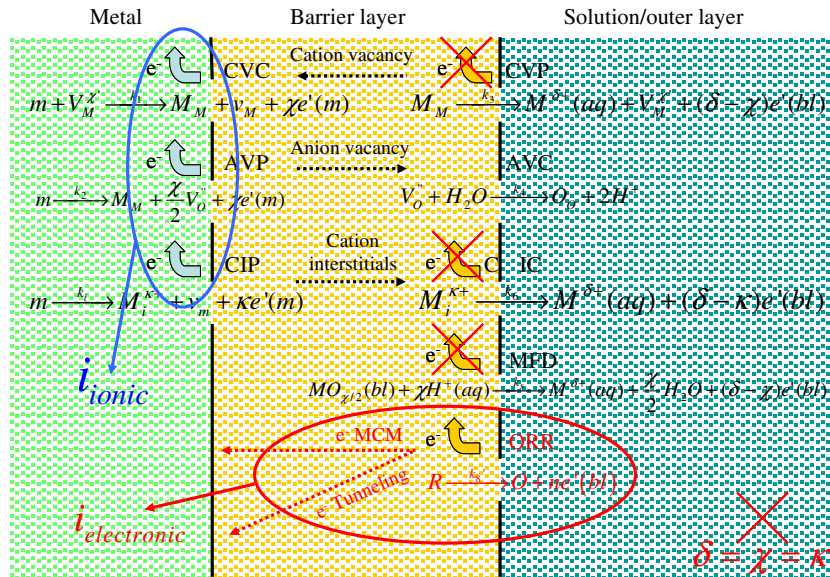


Fig. 7. Picturing the electron transport into the substrate: ionic and electronic contributions. Reactions according to [6].

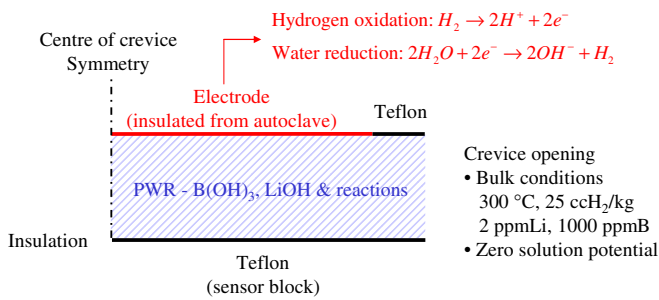


Fig. 8. Model for the autoclave crevice.

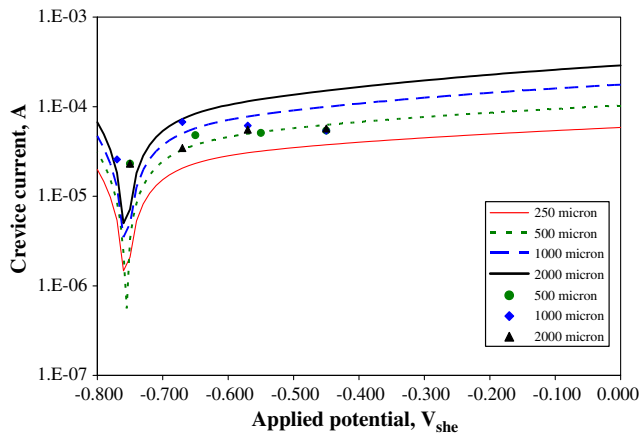


Fig. 9. Calculated (lines) and measured (symbols) crevice current versus applied potential for various crevice heights. The environmental conditions are 300 °C, 1–1000 ppmB, 2 ppmLi and 25 cc/kg (STP) dissolved hydrogen. Modelling information is given in Table 3.

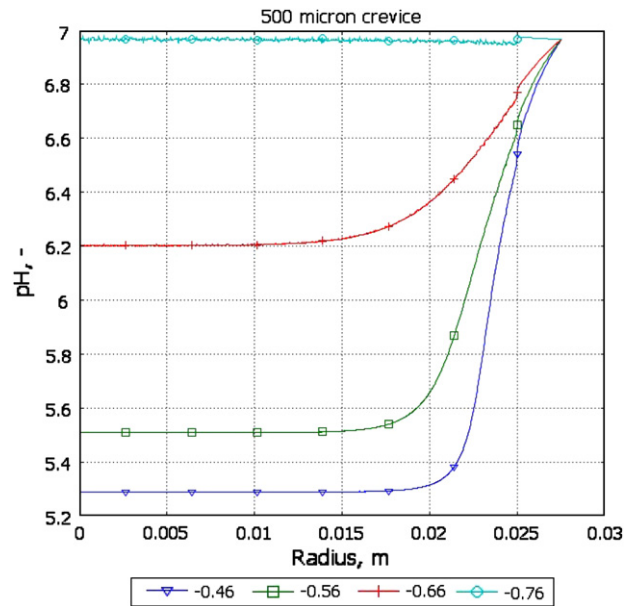


Fig. 10. Calculated pH profile in a 500 micron crevice at various applied potentials (OCP, OCP + 100 mV, OCP + 200 mV, OCP + 300 mV). The environmental conditions are 300 °C, 1000 ppmB, 2 ppmLi and 25 cc/kg (STP) dissolved hydrogen. Modelling information is given in Table 3.

- The radial pH profiles correspond to the conventional thinking with regard to acidification inside crevices. The higher the applied potential, the greater the acidification. There is no observable acidification at OCP where the crevice current is negligibly small.

- The radial potential profiles correspond to the conventional thinking with regard to a potential drop into the crevice and a largest potential gradient close to the mouth of the crevice. The higher the applied potential the greater the potential drop into the crevice and the greater the potential gradient close to the mouth of the crevice. The centre of the crevice is close to the so-called limiting conditions. There is no observable potential drop at OCP where the crevice current is negligibly small.

## 6. Comparison of measurements and calculation

In Fig. 9 the calculated and measured crevice current are plotted against the applied potential. The solid lines correspond to the

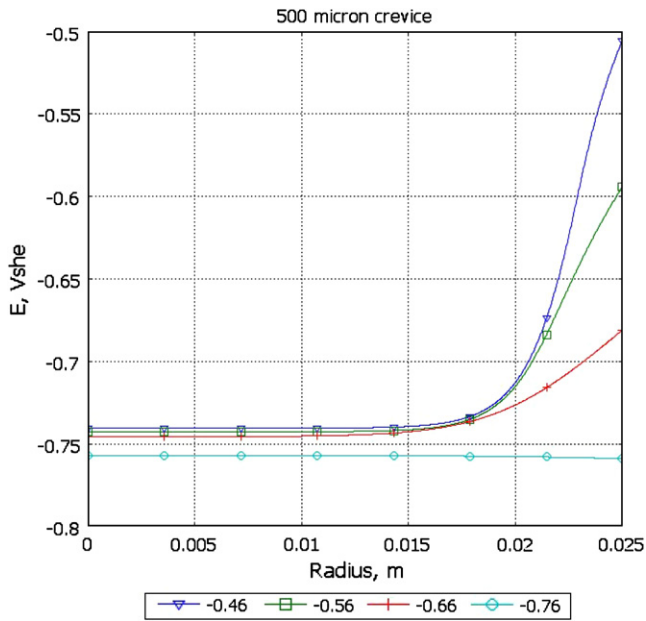


Fig. 11. Calculated electrode potential profile in a 500 µm crevice at various applied potentials (OCP, OCP + 100 mV, OCP + 200 mV, OCP + 300 mV). The environmental conditions are 300 °C, 1000 ppmB, 2 ppmLi and 25 cc/kg (STP) dissolved hydrogen. Modelling information is given in Table 3.

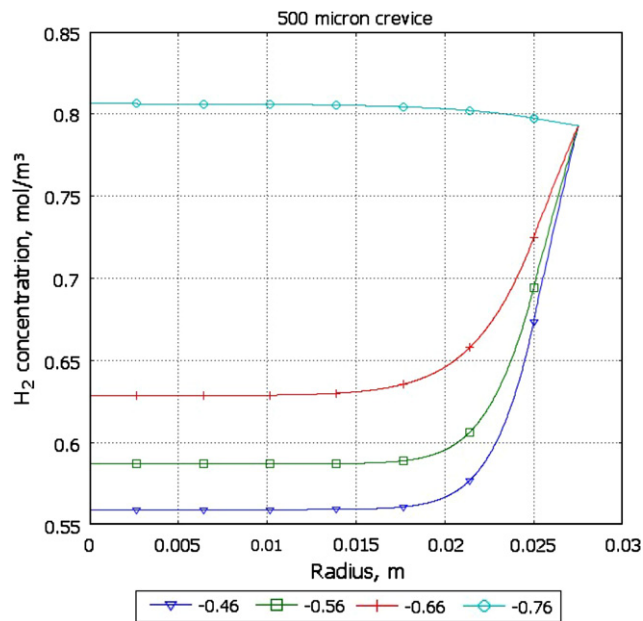


Fig. 12. Calculated hydrogen concentration profile in a 500 µm crevice at various applied potentials (OCP, OCP + 100 mV, OCP + 200 mV, OCP + 300 mV). The environmental conditions are 300 °C, 1000 ppmB, 2 ppmLi and 25 cc/kg (STP) dissolved hydrogen. Modelling information is given in Table 3.

calculation and the symbols to experimental measurements. The calculated crevice currents increase with the crevice height. This has to be understood as meaning that the resistance of the crevice interior to current transport is decreased as the crevice height increases. The calculated crevice currents lie above the measured ones and this is believed to be due to the fact that the external environment – and hence its resistance to current transport – has not been modelled. However, the agreement is reasonable, given that we have used data from various independent sources in the modelling and given the accuracy of the experimental measurements.

In Fig. 13, calculated and measured electrode potential profiles along the crevice are compared. The solid lines correspond to the calculated electrode potential profiles. These are plotted as calculated. The symbols indicate the measured platinum sensor potentials. These are plotted after correction. The corrections for Fig. 13 entail a pH correction, a conversion to the standard hydrogen scale (SHE) and a correction for IR-drop as detailed in Appendix B. The colour coding is blue for comparison at OCP, green for an applied potential of OCP + 100 mV, red for an applied potential of OCP + 200 mV and black for an applied potential of OCP + 300 mV.

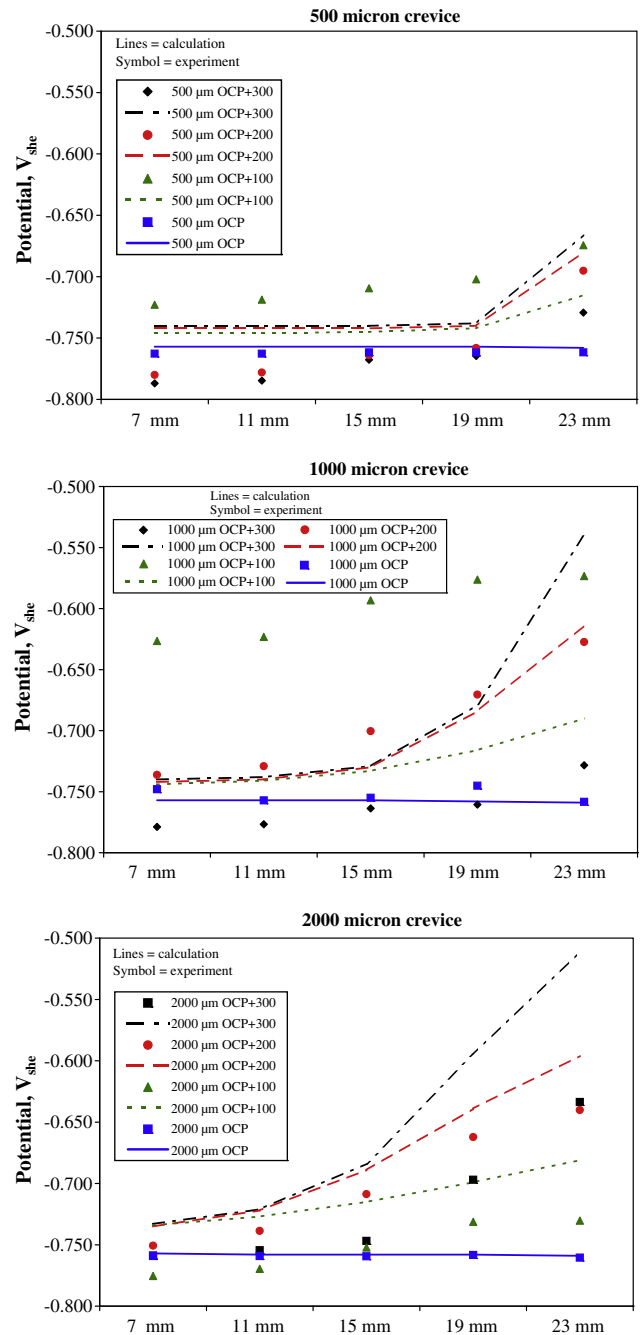


Fig. 13. Comparison of calculated (lines) and measured (symbols) electrode potential profiles in crevices of various heights (500, 1000 and 2000 µm), at various applied potentials (OCP, OCP + 100 mV, OCP + 200 mV, OCP + 300 mV). The environmental conditions are 300 °C, 1000 ppmB, 2 ppmLi and 25 cc/kg (STP) dissolved hydrogen. Modelling information is given in Table 3.

The measured crevice current and an Ohmic resistance of 5000  $\Omega$  are used in the IR-drop correction. Given that we have used data from various sources in the modelling and given the corrections needed, the agreement between measured and calculated potential profiles is reasonably good.

## 7. Conclusions

- Experimental electrode kinetic measurements have been performed on 316 stainless steel cylinders exposed to PWR-relevant conditions: 1000 ppmB, 2 ppmLi, 25 STP ccH<sub>2</sub>/kg at 300 °C. Fitting of the potentiostatic data yielded the following electrokinetic expression for the hydrogen oxidation reaction (H<sub>2</sub> → 2H<sup>+</sup> + 2e<sup>-</sup>) under long-term steady state conditions

$$i_{HR} = 1.682[H_2] \exp\left(\frac{0.20FE}{RT}\right).$$

- Autoclave crevice experiments have been performed under the same bulk conditions. The experimental measurements have been interpreted and evaluated using finite element computations of the electrochemistry in the crevice using hydrogen oxidation and water reduction as dominant electrochemical reactions.
- The relatively good agreement between the platinum sensors' potential measurements on the one hand and, the computational electrochemistry-calculated potentials on the other hand, indicates that the electrokinetic equations for hydrogen oxidation and water reduction are valid under the given operating conditions.

## Acknowledgements

The work has been performed at SCK-CEN and has been partially sponsored by Electrabel under contract number Convention KNT 90031700 and the European Union's 6th Framework Program Integrated Project 'Perfect' under contract number FI60-CT-2003-508840. The authors wish to express their gratitude to Ludo Eysermans and Rik-Wouter Bosch for their technical assistance.

## Appendix A. Electrode kinetic model

The mixed potential model [8] states that the total current density at an electrode is the sum of the anodic and cathodic current densities, i.e.

$$i_{total}(E) = i_{anodic}(E) + i_{cathodic}(E). \quad (3)$$

The open circuit potential can be derived from this equation by setting the total current to zero, i.e.

$$i_{anodic}(OCP) + i_{cathodic}(OCP) = 0. \quad (4)$$

The cathodic current density can be expressed as

$$i_{cathodic} = i_c e^{-\frac{\alpha_c F E}{RT}}, \quad (5)$$

when assuming only one cathodic reaction.

The anodic current density is the sum of the ionic and electronic current densities as shown in Fig. 7, i.e.

$$i_{anodic} = i_{ionic} + i_{electronic}. \quad (6)$$

According to the point defect model [11] the ionic current density is given by (Fig. 7)

$$i_{ionic} = i_{CVC} + i_{AVP} + i_{CIP}. \quad (7)$$

The subscripts, respectively, refer to cation vacancy consumption, anion vacancy production and cation interstitial production (Fig. 7).

The electronic current density is associated with the transport of electrons produced by the charge transfer reactions at the film/solution interface and subsequently transported to the substrate through the oxide film as shown in Fig. 7. When the film is thin the electrons can be tunneled [10] through the film and the resistance of the film is relatively low. However, when the film becomes thicker, electrons are transported as in semi-conductors [9] and the resistance of the film is relatively high. The change in transport mode can be described by the tunnelling equation [10]

$$i = \hat{i}_0 e^{-\beta L}. \quad (8)$$

The final Eqs. (9)–(12) are similar to a previously described Weibull transition between the active and passive state [12].

$$i_{electronic} = w \cdot i_a^{act} + (1 - w) \cdot i_a^{pass}, \quad (9)$$

$$w = \begin{cases} 1 & E < E_{flade}, \\ e^{-\left(\frac{E - E_{flade}}{E_{scale}}\right)^n} & E > E_{flade}, \end{cases} \quad (10)$$

$$i_a^{act} = i_a^{0,act} [H_2] e^{\frac{\alpha_a^{act} F E}{RT}}, \quad (11)$$

$$i_a^{pass} = i_a^{0,pass} [H_2] e^{\frac{\alpha_a^{pass} F E}{RT}}. \quad (12)$$

The correspondence between the empirical Weibull and the scientific tunnelling approaches can be derived by comparing Eqs. (8) and (10). One obtains

$$\beta L = \left[ \left( \frac{E_0}{E_{scale}} \right)^n \frac{\varepsilon}{(1 - \alpha) E_0} \right] \left[ \frac{(1 - \alpha) E_0}{\varepsilon} \left( \frac{E - E_{flade}}{E_0} \right)^n \right], \quad (13)$$

where  $E_0$  is arbitrary taken as 1 V. Assuming the following relation between potential and film thickness (14), which is a slight modification of the linear potential versus thickness relation given in [11]

$$L = \frac{(1 - \alpha) E_0}{\varepsilon} \left( \frac{E - E_{flade}}{E_0} \right)^n, \quad (14)$$

one gets the anodizing constant as

$$\beta = \left( \frac{E_0}{E_{scale}} \right)^n \frac{\varepsilon}{(1 - \alpha) E_0}. \quad (15)$$

The value of  $E_0$  has not been experimentally verified but could be on the basis of film thickness,  $\alpha$  and  $\varepsilon$  measurements. The value of  $n$  could be simultaneously obtained from a potential dependence of the film thickness. Since Eq. (14) is only used for illustrative purposes, to get an estimate of film thickness, and, hence, does not affect other conclusions, the authors can pick up the issue in future research.

When fitting the above model to the experimental potentiostatic polarization data shown in Figs. 1–5, the constants shown in Tables 1 and 2 are obtained. The cathodic parameters ( $i_c$  and  $\alpha_c$ ) were obtained from previous fitting of the cathodic part of polarization curves. Here, the parameters of the anodic parameters ( $i_a^{0,act}$ ,  $\alpha_a^{act}$ ,  $i_a^{0,pass}$  and  $\alpha_a^{pass}$ ) and the Weibull parameters ( $E_{flade}$ ,  $E_{scale}$  and  $n$ ) have been fitted to the anodic part. On the basis of the tunnelling current the anodizing constant  $\beta$  (15) has been obtained and is given in Table 1. It is interesting to note that data pertaining to various dissolved hydrogen concentrations could be fitted in one go – only the transition potential  $E_{trans}$  had to be varied with the dissolved hydrogen concentration (Table 2). The transition potential  $E_{trans}$  is shown in Table 2 as a function of the dissolved hydrogen concentration. The film thickness  $L$  has been calculated on the basis of Eq. (14) and it is also shown in Figs. 1–5.

**Table 1**

Summary of the various parameters and properties as used or obtained by modelling the experimental potential–current density data for 316 stainless steel in a nominal boric acid–lithium hydroxide solution (1000 ppmB, 2 ppmLi and 0–31.5 ccH<sub>2</sub>/kg) at 300 °C

Cathodic	$i_c$ (A/m <sup>2</sup> )	$6.47 \times 10^{-8}$ (from previous work)	
	$\alpha_c$ (-)	0.90 (from previous work)	
Anodic	Active	$i_a^{0,act}$ (A/m <sup>2</sup> )	2.00 (fitted in this work)
		$\alpha_a^{act}$ (-)	0.35 (fitted in this work)
	Passive	$i_a^{0,pas}$ (A/m <sup>2</sup> )	0.05 (fitted in this work)
		$\alpha_a^{pas}$ (-)	0.20 (fitted in this work)
Weibull transition(e <sup>-</sup> tunnelling ↔ e <sup>-</sup> mixed conduction)	$E_{nade}$ (V <sub>she</sub> )	$f(H_2)$ – see Table 2	
	$E_{scale}$ (V <sub>she</sub> )	0.100 (fitted in this work)	
	$n$ (-)	3.00 (fitted in this work)	
Film thickness	$\epsilon$ (V/m)	10 <sup>8</sup> (assumed)	
	$\alpha$ (-)	0.25 (assumed)	
	$\beta$ (/m)	$1.3 \times 10^{11}$ (calculated from Eq. (15))	

**Table 2**

Variation of the fitted transition potential,  $E_{nade}$ , as a function of the dissolved hydrogen concentration for 316 stainless steel in a nominal boric acid–lithium hydroxide solution (1000 ppmB, 2 ppmLi and 0–31.5 ccH<sub>2</sub>/kg) at 300 °C

[H <sub>2</sub> ] (cc/kg)	$E_{nade}$ (V <sub>she</sub> )
31.5	-0.570
26	-0.580
22	-0.650
17	-0.700
None (2)	-0.700

## Appendix B. Corrections to potential measurements

### B.1. Conversion to the standard hydrogen scale (SHE)

The platinum sensor (Pt) and specimen (WE) potentials are measured against an internal reference electrode and, hence, have to be converted to the standard hydrogen scale. The bulk pH at 300 °C for a solution containing 1000 ppmB and 2 ppmLi is 6.95. At 300 °C and a pH of 6.95 the conversion is -730 mV [7], i.e.

$$E_{she}^{Pt/WE}(V_{she}) = E_{ire}^{Pt/WE} + E_{she}^{ire} = E_{ire}^{Pt/WE}(\text{measured}) - 0.730V_{she}^{ire} \quad (16)$$

The specimen potentials at OCP are in the range -20 mV<sub>ire</sub> to -40 mV<sub>ire</sub>, and, hence, yield about -750 mV<sub>she</sub> to -770 mV<sub>she</sub> on the standard hydrogen scale. This OCP value is close to the finite element calculated OCP (Fig. 9).

### B.2. pH correction

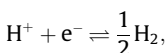
The platinum sensors measure a potential which is pH dependent. Hence, experimentally we cannot measure potential and pH separately. However, the modelling results give us the pH values at the respective platinum sensor locations. These can be used to pH-correct the measured platinum sensor potentials as follows:

$$E = E_{ire}^{measured} + E_{she}^{ire} + E_{pH}^{correction}$$

$$E = E_{ire}^{measured} + (-0.730V_{she}^{ire}) + \left[ 2.303 \frac{RT}{F} (\text{pH}^{calc} - \text{pH}_{ref}) \right]$$

where  $\text{pH}_{ref} = 6.95$

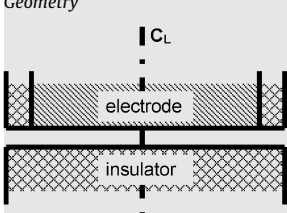
The factor  $2.303 \frac{RT}{F}$  comes from the pH dependence of the redox potential for the hydrogen reaction



which takes place at the platinum sensor surfaces. The factor can be derived from the Nernst equation for the hydrogen reaction, i.e.

**Table 3**

Data used for modelling the autoclave crevice

Geometry	Height	Radius	Variable
			Electrode 25 mm Outer 27.5 mm
<b>Conditions</b>			
Temperature	300 °C, 573 K	Pressure	150 bar
Density	711 kg/m <sup>3</sup>	Flow	None
Boron	1000 ppm, 65.77 mol/m <sup>3</sup>	Lithium	2 ppm, 0.20 mol/m <sup>3</sup>
pH	6.97	Conductivity	0.0522 S/m
<b>Ion system</b>			
Species	Charge	Diffusion coefficient (m <sup>2</sup> /s)	Bulk concentration (mol/m <sup>3</sup> )
1	Li <sup>+</sup>	$5.16 \times 10^{-8}$	0.2026
2	LiOH	$4.00 \times 10^{-8}$	$1.528 \times 10^{-5}$
3	LiB(OH) <sub>4</sub>	$4.00 \times 10^{-8}$	$9.319 \times 10^{-5}$
4	B(OH) <sub>3</sub>	$4.00 \times 10^{-8}$	65.57
5	B(OH) <sub>4</sub> <sup>-</sup>	$5.29 \times 10^{-8}$	0.1543
6	B <sub>2</sub> (OH) <sub>7</sub> <sup>-</sup>	$4.50 \times 10^{-8}$	$1.984 \times 10^{-2}$
7	B <sub>3</sub> (OH) <sub>10</sub> <sup>-</sup>	$3.57 \times 10^{-8}$	$1.573 \times 10^{-3}$
8	H <sup>+</sup>	$4.63 \times 10^{-7}$	$7.6871 \times 10^{-5}$
9	OH <sup>-</sup>	$2.63 \times 10^{-7}$	$2.695 \times 10^{-2}$
10	H <sub>2</sub>	$8.21 \times 10^{-8}$	0.793
Conductivity (S/m)			$\kappa = \frac{F^2}{RT} \sum_i z_i^2 D_i C_i$
<b>Electrochemical reactions</b>			
Reaction	Equation/parameters $E = V_m - \phi$		
H <sub>2</sub> → 2H <sup>+</sup> + 2e <sup>-</sup>	$i_{HR}(\text{A/m}^2) = 1.682[\text{H}_2] \exp\left(\frac{0.20FE}{RT}\right)$		
2H <sub>2</sub> O + 2e <sup>-</sup> → 2OH <sup>-</sup> + H <sub>2</sub>	$i_{WR}(\text{A/m}^2) = -6.47 \times 10^{-8} \exp\left(-\frac{0.90FE}{RT}\right)$		
Species No.	Flux (injection is positive)		
8	$i_{HR}/F$		
9	$-i_{WR}/F$		
10	$-i_{WR}/(2F) - i_{HR}/(2F)$		
<b>Chemical reactions</b>			
Reaction	$k_f$ (for mol/m <sup>3</sup> )	$k_b$ (for mol/m <sup>3</sup> )	$K_{eq} (=k_f/k_b \text{ for mol/m}^3)$
1	B(OH) <sub>3</sub> + OH <sup>-</sup> ↔ B(OH) <sub>4</sub> <sup>-</sup>	1	11.45
2	B(OH) <sub>4</sub> <sup>-</sup> + B(OH) <sub>3</sub> ↔ B <sub>2</sub> (OH) <sub>7</sub> <sup>-</sup>	$1.960 \times 10^{-3}$	1
3	B <sub>2</sub> (OH) <sub>7</sub> <sup>-</sup> + B(OH) <sub>3</sub> ↔ B <sub>3</sub> (OH) <sub>10</sub> <sup>-</sup>	$1.210 \times 10^{-3}$	1
4	Li <sup>+</sup> + OH <sup>-</sup> ↔ LiOH	$2.789 \times 10^{-3}$	1
5	Li <sup>+</sup> + B(OH) <sub>4</sub> <sup>-</sup> ↔ LiB(OH) <sub>4</sub>	$2.982 \times 10^{-3}$	1
w	H <sub>2</sub> O ↔ H <sup>+</sup> + OH <sup>-</sup>	1	482732
Species number	Production rate		
1	$(k_{4b} \cdot c_2 - k_{4f} \cdot c_1 \cdot c_9) + (k_{5b} \cdot c_3 - k_{5f} \cdot c_1 \cdot c_5)$		
2	$k_{4f} \cdot c_1 \cdot c_9 - k_{4b} \cdot c_2$		
3	$k_{5f} \cdot c_1 \cdot c_5 - k_{5b} \cdot c_3$		
4	$(k_{1b} \cdot c_5 - k_{1f} \cdot c_4 \cdot c_9) + (k_{2b} \cdot c_6 - k_{2f} \cdot c_4 \cdot c_5) + (k_{3b} \cdot c_7 - k_{3f} \cdot c_4 \cdot c_6)$		
5	$(k_{1f} \cdot c_4 \cdot c_9 - k_{1b} \cdot c_5) + (k_{2f} \cdot c_4 \cdot c_5 - k_{2b} \cdot c_6) + (k_{3f} \cdot c_4 \cdot c_6 - k_{3b} \cdot c_7)$		
6	$(k_{2f} \cdot c_4 \cdot c_5 - k_{2b} \cdot c_6) + (k_{3b} \cdot c_7 - k_{3f} \cdot c_4 \cdot c_6)$		
7	$k_{3f} \cdot c_4 \cdot c_6 - k_{3b} \cdot c_7$		
8	$(k_{wf} - k_{wb} \cdot c_8 \cdot c_9)$		
9	$(k_{wf} - k_{wb} \cdot c_8 \cdot c_9) + (k_{4b} \cdot c_2 - k_{4f} \cdot c_1 \cdot c_9) + (k_{1b} \cdot c_5 - k_{1f} \cdot c_4 \cdot c_9)$		
10	0		

The experimental environmental conditions are 300 °C, 1000 ppmB, 2 ppmLi and 25 cc/kg (STP) dissolved hydrogen.

$$E_{HR} = E_{HR}^0 - \frac{RT}{F} \ln(H^+) = E_{HR}^0 - 2.303 \frac{RT}{F} \log_{10}(H^+) = E_{HR}^0 + 2.303 \frac{RT}{F} \text{pH}.$$



The reference pH value,  $\text{pH}_{\text{ref}}$ , is subtracted from the calculated pH,  $\text{pH}^{\text{calc}}$ , for the  $E_{\text{she}}^{\text{ire}}$  value of  $-0.730V_{\text{she}}^{\text{ire}}$  already took into account a pH of 6.95. The factor's value at 300 °C is 0.1139.

### B.3. IR-drop correction

The absolute values of measured (pH-corrected) and calculated potential profiles differ when a potential is applied to the tested specimen (i.e. OCP + 100 mV and OCP + 200 mV). This lead us to believe that an IR-drop correction was needed. The finale correction then reads

$$E = E_{\text{ire}}^{\text{measured}} + E_{\text{she}}^{\text{ire}} + E_{\text{pH}}^{\text{correction}} + E_{\text{IR}}^{\text{correction}},$$

$$E = E_{\text{ire}}^{\text{measured}} + (-0.730V_{\text{she}}^{\text{ire}}) + [0.1139(\text{pH}^{\text{calc}} - \text{pH}_{\text{ref}})] + I \cdot R,$$

where  $\text{pH}_{\text{ref}} = 6.95$ .

A value of 5000  $\Omega$  has been used for the solution resistance throughout all the experiments. The correction is thought to be needed for/related to (1) the position of the IRE, which is away from the crevice mouth and (2) neglecting the external environment in the modelling.

## References

- [1] P.L. Andresen, in: R.H. Jones (Ed.), Stress-corrosion Cracking, ASM International, 1992, ISBN 0-87170-441-2.
- [2] P. Scott, J. Nucl. Mater. 211 (1994) 101.
- [3] P.L. Andresen et al., Proceedings of the International Conferences on Nuclear Reactor Engineering, vol. 5, ASME, 1996, p. 461.
- [4] D.D. Macdonald et al., Corrosion 52 (10) (1996) 768.
- [5] T. Satoh et al., J. Nucl. Sci. Technol. 38 (9) (2001) 773.
- [6] M. Schneider, K. Nocke, H. Worch, Mater. Corros. 51 (2000) 545.
- [7] R.W. Bosch, D. Féron, J.P. Celis, Electrochemistry in light water reactors: reference electrodes, measurements, corrosion and tribocorrosion issues, EFC Publication No. 49, Woodhead Publishing in Materials, Cambridge, England, 2007.
- [8] D.L. Piron, The Electrochemistry of Corrosion, NACE International, 1994, ISBN 1-877914-23-1.
- [9] M. Bojinov et al., J. Electroanal. Chem. 504 (2001) 29.
- [10] M. Kamrunnihar, J. Bao, D.D. Macdonald, Corros. Sci. 47 (2005) 3111.
- [11] D.D. Macdonald, J. Electrochem. Soc. 139 (12) (1992) 3433.
- [12] M. Vankeerberghen, M. Abdulsalam, H. Pickering, J. Deconinck, J. Electrochem. Soc. 150 (9) (2003) B445.
- [13] J.S. Newman, Electrochemical Systems, 2nd ed., Prentice-Hall, 1991, ISBN 0-13-248758-6.